
DATA-DRIVEN SPARSE MODELING AND DECOMPOSITION FOR SUPERSPREADING-WETTING DYNAMICS OF A DROPLET

A PREPRINT

Kai Fukami

Department of Aerospace Engineering
Graduate School of Engineering
Tohoku University
Sendai, 980-8579, Japan
kfukami1@tohoku.ac.jp

Eita Shoji

Department of Mechanical Systems Engineering
Graduate School of Engineering
Tohoku University
Sendai, 980-8579, Japan
eita.shoji@tohoku.ac.jp

January 6, 2026

ABSTRACT

Superspreading wetting is traditionally attributed to surfactant-driven mechanisms. However, recent observations of superspreading in surfactant-free nanofluids defy standard theoretical explanations. This study considers a data-driven approach to model droplet dynamics with the thickness of liquid films on the nanometer-micrometer scale in a compact form of a partial differential equation. We examine spatiotemporal film-thickness profiles resolved at the nanometer scale via phase-shifting imaging ellipsometry. For a pure solvent, the present governing equation recovers the classical lubrication physics driven by disjoining pressure and evaporation. In contrast, the nanofluid dynamics necessitates a unique transport term scaling with the gradient of the inverse film thickness. Theoretical analysis suggests this term represents a nanoparticle-induced bias flux, consistent with a hypothesized capillary wicking mechanism within the precursor film. The identification of the current nanofluid-specific term underscores the efficacy of integrating high-precision experimental measurements with data-driven modeling to unravel complex wetting dynamics.

1 Introduction

Fluid mechanicians have admired the rich physics of superspreading wetting, initiated by the discovery in Schwarz & Reid (1964) [1]. First identified in surfactant-laden aqueous drops, superspreading is characterized by significant deviations from the simple scaling law between contact radius and time [2]. However, the underlying spreading mechanism remains elusive, making it challenging to universally capture their transient, material-dependent characteristics [3].

Beyond these surfactant-based systems, our recent experiments revealed that surfactant-free nanofluids composed of highly dispersed, single-nanometer particles also exhibit superspreading [4]. Comprehensive characterization has systematically ruled out conventional mechanisms: surface tension measurements negated Marangoni and bilayer effects [5, 6], while time-resolved droplet shape analysis excluded structural disjoining pressure [7]. Furthermore, the observed shear-thickening rheology [8] contradicts spreading models based on viscosity reduction. Consequently, establishing a mechanistic description for this anomalous wetting dynamics—unexplainable by standard theories—is a challenge.

The key to unlocking this mechanism lies in the nanometric precursor film. Indeed, both the bilayer structures proposed for surfactants [6] and the nanoparticle persistence observed in our experiments [4] point to this microscopic region as the origin of the superspreading force. While classical theories provide a framework for precursor film dynamics [9, 10], their experimental validation has mostly relied on high-viscosity, non-volatile liquids where slow dynamics permit conventional measurements. In contrast, capturing the fast, transient evolution of precursor films remains experimentally challenging. To address this, we utilize phase-shifting imaging ellipsometry, which has been developed to spatiotemporally resolve nanometer-thick precursor films [11]. However, deducing the specific mechanism driving superspreading solely from such kinematic profiles remains difficult via traditional reasoning.

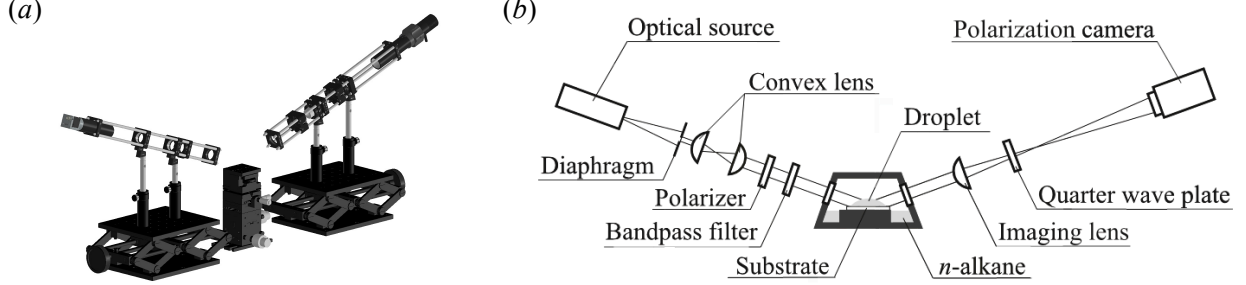


Figure 1: The phase-shifting imaging ellipsometer and sealed environmental cell used in the present analysis: (a) the model and (b) detailed descriptions are shown. The optical configuration and calibration/uncertainty procedures are identical to our prior studies [11, 4].

To bridge this gap, this study considers a data-driven approach to infer the operative dynamics directly from these measurements. We aim to model droplet dynamics with the thickness of liquid films on the nanometer-micrometer scale as a form of a parametric partial differential equation. This is achieved by a data-driven sparse modeling approach, PDE-FIND [12]. Equipped with sparsity-promoting optimizations, the algorithm enables discovering a modeled equation from time-discretized data while identifying dominant terms from a set of potential term candidates that are likely to be involved in the model, referred to as a library [13]. Combining with other data-driven techniques such as nonlinear machine-learning-based reduced-order modeling [14, 15], such sparsity-promoting data-driven approaches have been used for prediction and control of a range of scientific and engineering problems. Examples include robotics [16], biology [17], solid mechanics [18], and unsteady aerodynamics [19, 20].

Focusing on the dynamics of liquid-film thickness under a superspreading wetting condition, this study finds that their dynamics can be expressed in a much sparser form than expected — a set of effects for pressure diffusion, evaporation, and bias flux. Furthermore, this study discusses how very local effects under the micrometer height are identified with the present technique in a physically interpretable manner.

This paper is organized as follows. The approach is described in section 2. Results of model discovery for the micrometer-thick liquid film data sets are presented in section 3. Conclusions are offered in section 4.

2 Approach

This study aims to extract physical insights from experimental data on superspreading nanofluids through sparse dynamical modeling. We consider previously published experimental data [4], acquired via phase-shifting imaging ellipsometry shown in figure 1. The capability of this technique to resolve nanoscale precursor film dynamics has been demonstrated across various wetting phenomena, ranging from particle suspensions [21] to evaporating nanofluids [22]. This setup enables measuring spatiotemporal thickness fields from nanometric to micrometric scales. We examine two liquids: pure *n*-heptane and a surfactant-free 5 wt% nanofluid containing surface-modified CeO₂ nanoparticles dispersed in *n*-heptane. Silicon wafers served as substrates, with surface preparation and optical modeling. The environmental cell was saturated with the working liquid to suppress evaporation.

Representative flow snapshots visualized as the phase difference distribution φ between *p*- and *s*-polarizations are presented in figure 2, where the observed interference fringes serve as topographic contours of the liquid film. Along with these snapshots, the corresponding radial thickness profiles $h(r, t)$ are plotted. The insets in the thickness plots highlight the dynamics within the nanometric precursor region ($h \lesssim 10^{-7}$ m), specifically focusing on the timeframes where the distinct behaviors become most pronounced: $t > 320$ s for the pure liquid, where spreading is arrested by evaporation, and $t > 450$ s for the nanofluid, where superspreading becomes dominant. This pairing serves as a testbed for data-driven discovery. That is, the pure liquid validates the method against classical lubrication physics, while the nanofluid presents an unexplained dynamical anomaly. Crucially, our analysis targets this nanometric precursor region ($h \lesssim 100$ nm). Since our previous post-drying observations suggested that nanoparticles persist even within this precursor film region, we posit that the singular physics in this $O(10^{-7})$ m vicinity, governed by disjoining pressure and particle-induced effects, ultimately dictate the macroscopic spreading dynamics.

Equipped with the superspreading droplet datasets, we aim to identify a model equation of height dynamics as a form of partial differential equation, i.e., $h_t = \mathcal{N}(h, h_r, h_{rr}, \dots)$, where the temporal evolution of the height profile is expressed as a linear combination of nonlinear spatial derivatives, as summarized in figure 3. This is achieved with a data-driven technique, PDE-FIND [12], enabling the extraction of model equations from given time-series data in a

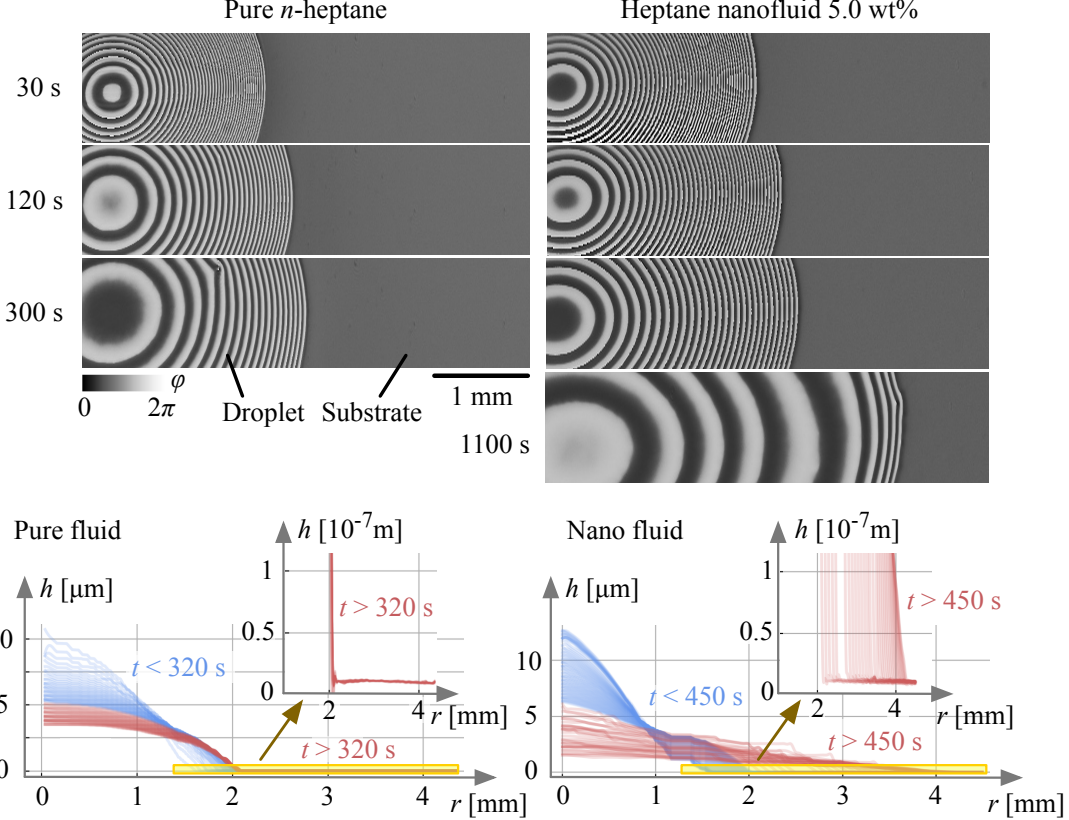


Figure 2: Phase difference field φ of the pure *n*-heptane and the heptane 5 wt% nanofluid along with their height dynamics. The zoomed-in view of the region of interest for the current data-driven analysis, highlighted with yellow boxes, is also shown.

sparse, parsimonious form. The PDE-FIND models the time-varying height dynamics as the superposition of candidate physical terms, referred to as the library matrix $\Theta(h)$ detailed later, with the weighting coefficients β , such that $\mathbf{H}_t = \Theta(h)\beta$. Given the discretized height data $h(r, t)$ measured at m spatial points and n temporal points, $\mathbf{H}_t \in \mathbb{R}^{mn}$ is the column vector of the temporal derivatives of height, and $\beta \in \mathbb{R}^D$ is the vector of coefficients for D library terms. Once the droplet dynamics is identified as a PDE form, it is also possible to examine the spatiotemporal pattern of each term appearing in the modeled equation, enabling us to capture the transient characteristics in a decomposed manner.

While generic polynomial expansions are often considered for library construction [13, 12], this study considers populating them based on our prior knowledge of droplet dynamics, derived from the lubrication approximation, segregated into regions dominated by intermolecular forces and those dominated by surface tension. We hereafter use $h_t \equiv \partial h / \partial t$ and $h_r \equiv \partial h / \partial r$ for compactness.

Considering the region of interest, the precursor region where disjoining pressure drives the flow, the library prioritizes terms scaling with negative powers of the film height. Specifically, we incorporate the divergence of the conservative flux for non-retarded van der Waals forces, $(h^{-1}h_r)_r$, alongside candidate terms for thinness-activated transport, such as $(h^{-1})_r$ and $(h^{-2})_r$. To enhance robustness against measurement noise and discretization errors, we also include expanded non-conservative derivatives, e.g., $h^{-1}h_{rr}$, and alternative formulations of the driving force, such as $(h^3\Pi_r)_r$, where $\Pi \propto h^{-3}$ represents the canonical disjoining pressure. The resulting full library matrix $\Theta(h)$ is expressed as

$$\Theta(h) = [1, h^{-3}, (h^{-1}h_r)_r, (h^{-1})_r, (h^{-2})_r, \dots, h^{-1}h_{rr}, (h^3\Pi_r)_r]. \quad (1)$$

Once the library matrix $\Theta(h)$ is defined, the coefficients for each term in the library are sought through the iterative optimization,

$$\beta^* = \operatorname{argmin}_{\beta} \|\Theta\beta - \mathbf{H}_t\|_2 + \alpha \|\beta\|_1, \quad (2)$$

where $(\cdot)^*$ represents the optimized variable. Here, the coefficients are determined through the sequential threshold least squares method [13], promoting sparsity of the coefficient matrix in a computationally tractable manner.

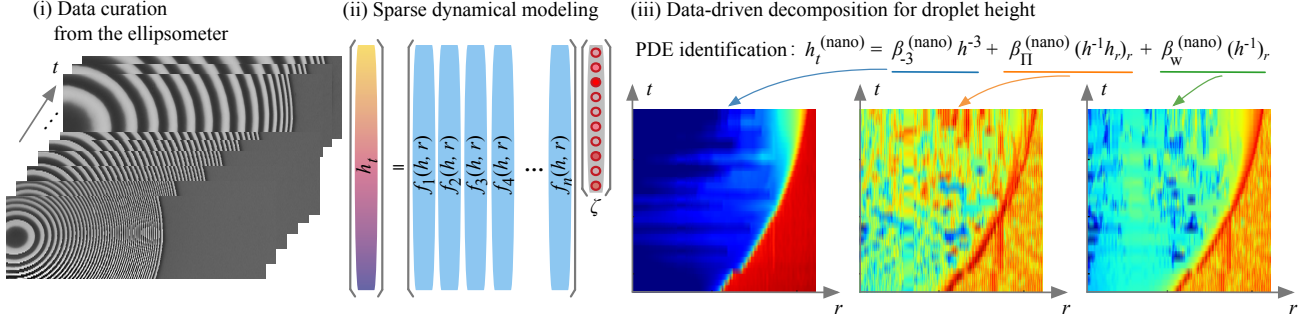


Figure 3: Overview of the present analysis: (i) Data curation from the ellipsometer, (ii) sparse dynamical modeling, and (iii) data-driven decomposition for the droplet height based on the modeled equations.

3 Results

Let us apply the current data-driven technique to the time-resolved thickness profiles of the nanoliquid film near the contact line to infer the local dynamics of the liquid-film thickness $h(r, t)$. The present approach finds the following sparse model forms for the pure *n*-heptane and the nanofluid:

Pure *n*-heptane:

$$h_t = -4.29 \times 10^{-16} - 5.18 \times 10^{-31} h^{-3} - 2.68 \times 10^{-19} (h^{-1}h_r)_r \quad (3)$$

Nanofluid (surface modified CeO₂ in *n*-heptane):

$$h_t = -8.23 \times 10^{-16} - 1.17 \times 10^{-31} h^{-3} - 7.26 \times 10^{-19} (h^{-1}h_r)_r + 2.63 \times 10^{-19} (h^{-1})_r \quad (4)$$

These two models share three terms of the constant, h^{-3} , and $(h^{-1}h_r)_r$, while one additional term of $(h^{-1})_r$ emerges for the nanofluid. This suggests that the $(h^{-1})_r$ term presents the effect of nanofluid injection, and we find that it is likely true from the comparison to the classical thin-film model, which is detailed later. Furthermore, this study reveals that the order of the identified coefficients provides physical insights on the time-varying characteristics of the superspreading-wetting dynamics of a droplet.

Let us focus on the terms that commonly appear in the identified models. The constant term can be viewed as the effect of near-saturated evaporation and condensation, based on a well-known planar lubrication thin-film model [23],

$$h_t = -\frac{1}{\rho_\ell} (j_0 + \Lambda p) + \partial_r \left(\frac{h^3}{3\mu} p_r \right), \quad p = \Pi(h) - \gamma \kappa, \quad \kappa \simeq h_{rr}, \quad (5)$$

where μ is the liquid viscosity, ρ_ℓ is the liquid density, γ is the liquid-air surface tension, κ is the mean curvature (approximated by h_{rr} for small slopes), j_0 is a nearly uniform residual vapour flux set by the slight undersaturation, and Λ is an effective pressure-evaporation coefficient. The disjoining pressure is expressed in the nonretarded van der Waals form $\Pi(h) = -A/(6\pi h^3)$, with Hamaker constant $A < 0$ for the present Si/SiO₂/*n*-heptane/air system. Comparison with this theoretical model reveals that the identified equations capture the phase change dynamics through two distinct source/sink terms: a constant term and a pressure-dependent term proportional to h^{-3} .

First, the constant term, denoted here as β_0 , captures the spatially uniform thinning rate $-j_0/\rho_\ell$. The identified values of $\beta_0 \sim \mathcal{O}(10^{-16}) \text{ m} \cdot \text{s}^{-1}$ represent the background evaporation rate due to slight undersaturation in the sealed cell. Integrated over the experimental timescale (10^4 s), this rate corresponds to a total thickness loss of only $\sim 10^{-12} \text{ m}$, which is negligible compared to the nanometric film thickness. This confirms the high fidelity of the environmental control, allowing us to treat the dynamics as effectively conservative with respect to the ambient atmosphere.

Second, the term proportional to h^{-3} (coefficient β_{-3}) captures the local modulation of evaporation by disjoining pressure. For the lubrication model in equation 5, this effect corresponds to the source term $-(\Lambda/\rho_\ell)\Pi(h)$. The coefficient Λ is physically linked to the accommodation coefficient α via the linearized Hertz-Knudsen relation for interface-limited kinetics, $J_{\text{evap}} \approx \alpha(\rho_v/\rho_\ell)\sqrt{M/(2\pi RT)}\Pi(h)$. Matching the identified coefficient β_{-3} with this theoretical form implies an effective accommodation factor of $\alpha \sim 10^{-2}$. Although the intrinsic accommodation coefficient for pure alkanes is typically close to unity, this lower effective value captures the combined effects of near-interface vapor diffusion resistance and the reduction of active surface area due to high nanoparticle concentration. The clear separation of these two evaporative modes, a negligible background rate and a physically reasonable pressure-coupled response, validates the physical fidelity of the sparse modeling.

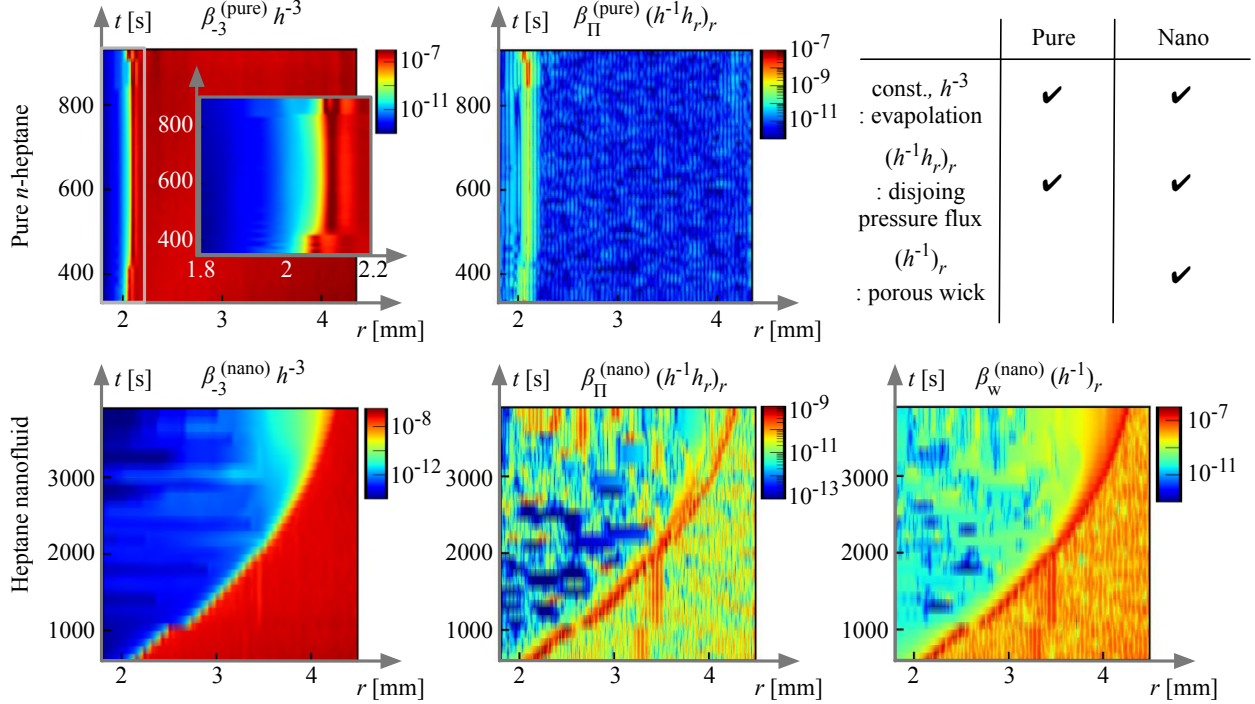


Figure 4: Data-driven decomposition of the droplet-height dynamics with a pure n -heptane and the heptane 5 wt% nanofluid. The absolute logarithmic value of each term in the identified equations is presented.

Furthermore, the term proportional to $(h^{-1} h_r)_r$, corresponding to the hydrodynamic flux driven by disjoining pressure, also appears in both of the identified models, as shown in equations 3 and 4. We find that the order of the coefficient makes sense from the viewpoint of droplet physics, while this term nicely highlights the difference between the pure and nano fluids as that in magnitude of the coefficient. Regarding the order of the coefficient, let us consider non-retarded van der Waals forces $\Pi(h) = -A/(6\pi h^3)$, providing the estimate of the coefficient as $\beta_{\Pi} = A/(6\pi\mu)$. For the Si/SiO₂/ n -heptane system, Lifshitz theory [24] predicts a Hamaker constant range of $A \simeq -(10^{-21}\text{--}10^{-20})$ J. Given the viscosity of n -heptane, this implies a theoretical coefficient range of $\beta_{\Pi}^{(\text{theory})} \sim -(10^{-19}\text{--}10^{-18})$ m³ s⁻¹. Our sparse modeling yields $\beta_{\Pi}^{(\text{pure})} \approx -2.7 \times 10^{-19}$ m³ s⁻¹ and $\beta_{\Pi}^{(\text{nano})} \approx -7.3 \times 10^{-19}$ m³ s⁻¹, both falling within this theoretical regime. These values correspond to effective Hamaker constants of $A_{\text{eff}}^{(\text{pure})} \approx -2.1 \times 10^{-21}$ J and $A_{\text{eff}}^{(\text{nano})} \approx -5.6 \times 10^{-21}$ J. Furthermore, the increment in magnitude, $|A_{\text{eff}}^{(\text{nano})}| > |A_{\text{eff}}^{(\text{pure})}|$, is physically consistent with the near-wall enrichment of CeO₂ nanoparticles. Since CeO₂ possesses a higher refractive index and dielectric constant than both n -heptane and SiO₂, its presence enhances the effective polarizability of the film, thereby strengthening the van der Waals attraction.

Let us now address the unique operator $(h^{-1})_r$ identified only in the nanofluid equation. This term represents a flux $J_{\text{bias}} \propto h^{-1}$, implying a transport mechanism that becomes increasingly effective as the film thins. Our previous measurements have found that nanoparticles persist within the nanometric precursor film [4]. To explain the physical origin of the $(h^{-1})_r$ term, we hypothesize that these particles locally accumulate near the contact line due to evaporation, forming a porous-like structure that exerts a wicking action. In this scenario, the rim generates a capillary suction $P_c \sim 2\gamma/r_{\text{eff}}$ and possesses a permeability k , creating a Darcy flux that drags the adjacent liquid film.

To evaluate the plausibility of this hypothesis, we estimate the theoretical magnitude of the transport coefficient β_w using the scaling $\beta_w^{(\text{theory})} \sim e(kH_p/\mu)P_c$, where H_p is the rim thickness and e is an efficiency factor. Given the uncertainty in the microscopic structure, we evaluate the theoretical range using a rim thickness $H_p \in [10, 50]$ nm and porosity $\varepsilon \in [0.1, 0.5]$. With the experimental properties ($d_p \simeq 6$ nm, $\gamma \simeq 20.2$ mN m⁻¹), the ideal wicking capacity $(kH_p P_c/\mu)$ spans a window of $\mathcal{O}(10^{-19})\text{--}\mathcal{O}(10^{-16})$ m³ s⁻¹. The identified coefficient $\beta_w \approx 2.6 \times 10^{-19}$ m³ s⁻¹ falls near the lower bound of this physically plausible range. This corresponds to an efficiency factor $e \sim 10^{-2}\text{--}10^{-1}$. Given the complexity of the coupled transport phenomena, including evaporation, nanoparticle migration, and the resulting local variations in the rim structure, this order of magnitude renders the hypothesis physically plausible. However, we emphasize that the capillary wicking model represents one possible physical interpretation of the identified $(h^{-1})_r$ flux. While the quantitative agreement offered by this model is compelling, the data-driven identification of the $(h^{-1})_r$ term

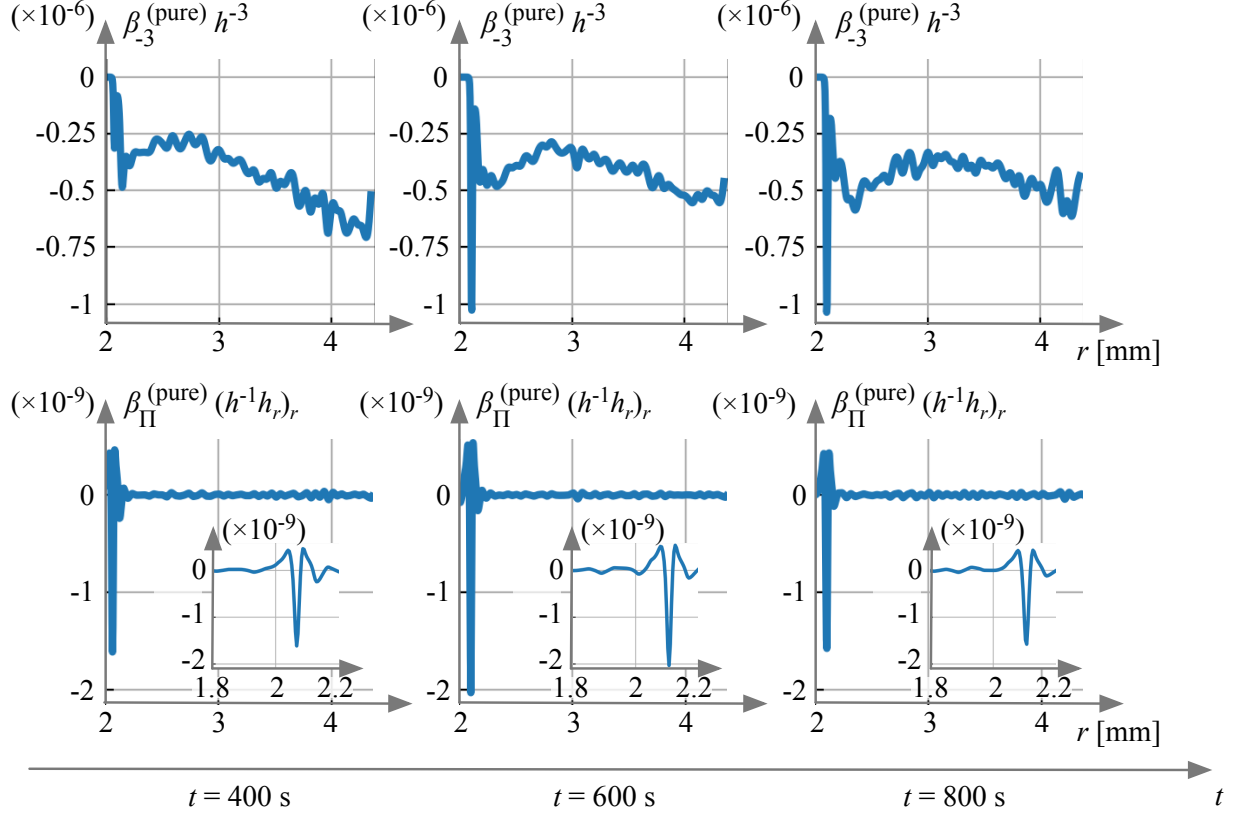


Figure 5: Time-varying contribution of the terms identified through the data-driven sparse modeling for the droplet height with a pure n -heptane.

does not preclude alternative mechanisms that might yield similar scaling laws. Nevertheless, the fact that the identified coefficient lies within a theoretically explainable range strongly supports the view that nanoparticle-induced structural effects are the primary driver of superspreading, warranting further mechanistic investigation.

To examine the dynamical balance of the identified mechanisms, let us present in figure 4 the magnitude of the local contribution from each operator. Here, we consider the global spatiotemporal evolution of the absolute values of these terms (log-scale) in the $r - t$ plane. The nanofluid significantly promotes the expansion speed and range in the r direction as the contact line is clearly observed, driven by all the identified terms. The pressure-coupled evaporation $\beta_{-3} h^{-3}$ contributes primarily in the thinnest regions, scaling naturally with film thickness. The disjoining flux $\beta_{\Pi} (h^{-1} h_r)_r$ exhibits high intensity specifically within the precursor film region throughout the spreading process, consistent with classical precursor film theory. Notably, the bias flux in the nanofluid, $\beta_w^{(\text{nano})} (h^{-1})_r$, also displays elevated values in this same spatial domain. The current observation that this term is active precisely where the precursor film exists is consistent with the hypothesis that nanoparticles within the nanoliquid film play a governing role in the superspreading dynamics.

Detailed spatial profiles for the pure n -heptane are shown in figure 5. Under the present saturated condition, a pre-existing adsorbed film (~ 10 nm) is present ahead of the spreading front. As the macroscopic spreading gradually arrests (at $t = 600$ and 800 s), the pressure-coupled evaporation term $\beta_{-3} h^{-3}$ exhibits a distinct, localized region of high negative intensity (large absolute value) at the transition zone ($r \approx 2.1$ mm) connecting the precursor to the adsorbed film. This indicates significant local thinning driven by evaporation, suggesting that this localized evaporative sink effectively pins the contact line, halting the expansion. Note that fluctuations in this term at larger radii merely reflect minor thickness variations in the adsorbed layer and lack physical significance. Concurrently, the disjoining pressure flux $\beta_{\Pi}^{(\text{pure})} (h^{-1} h_r)_r$ displays a characteristic spatial variation within this same transition region: as r increases, it exhibits a positive peak, followed by a prominent negative trough and a secondary positive peak, before asymptotically decaying to zero. This complex oscillatory structure likely arises from the intricate mass transport required to compensate for the strong local evaporation identified above. While the similarity of these profiles across different time steps is intriguing, a detailed stability analysis of this quasi-steady state remains a subject for future work.

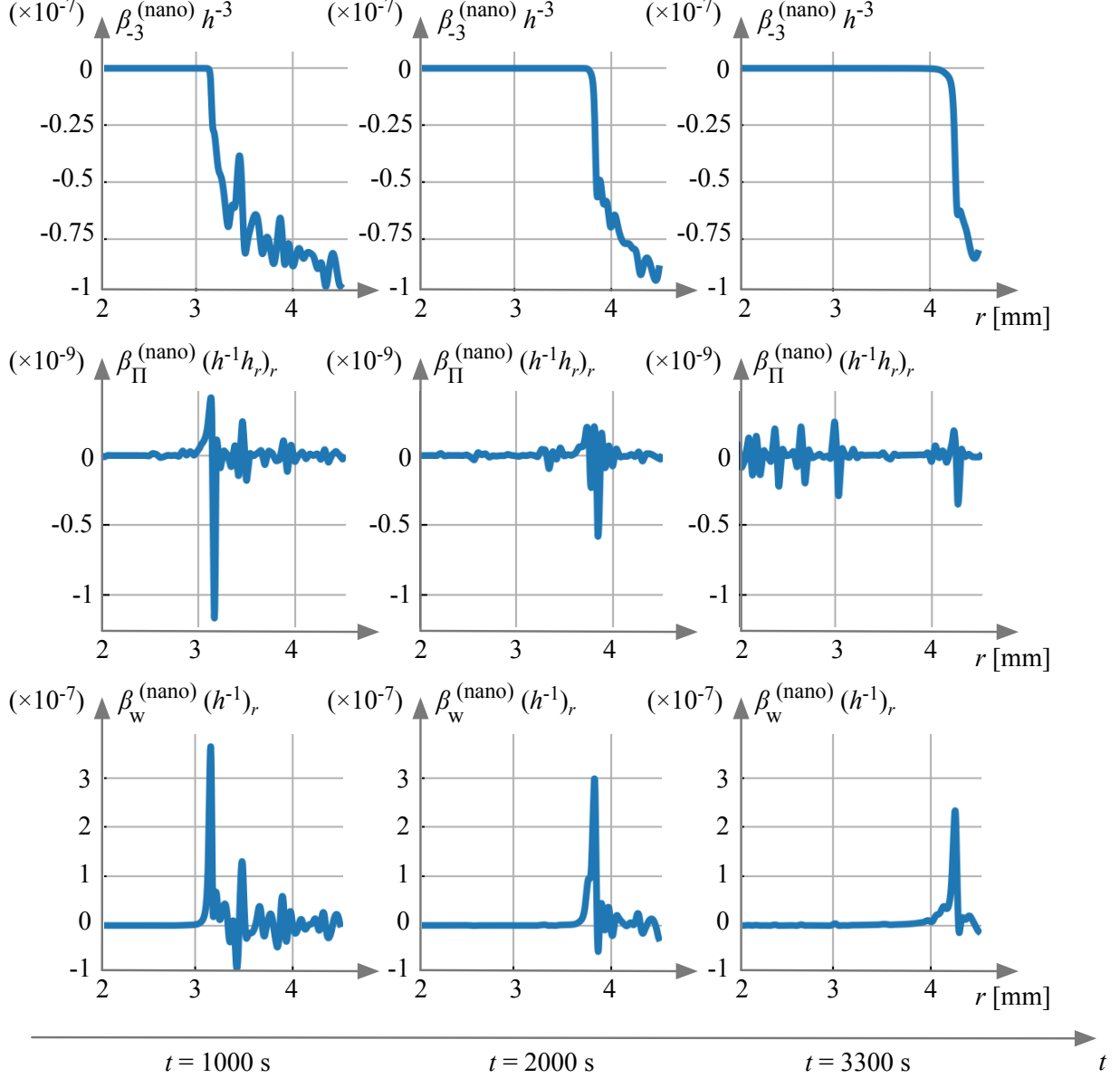


Figure 6: Time-varying contribution of the terms identified through the data-driven sparse modeling for the droplet height with the heptane 5 wt% nanofluid.

In contrast, the nanofluid dynamics, detailed in figure 6, exhibit a fundamental shift in the force balance. The pressure-coupled evaporation $\beta_{-3}h^{-3}$ follows a spatial distribution naturally scaling with film thickness, though its magnitude is approximately an order of magnitude lower than that of the pure *n*-heptane. The disjoining pressure flux $\beta_{\Pi}^{(\text{nano})}(h^{-1}h_r)_r$ retains a spatial structure similar to the pure case, showing elevated absolute values at the advancing transition zone connecting to the adsorbed film. However, its overall contribution is smaller than in the pure liquid. Instead, the dynamics are overwhelmingly governed by the nanofluid-specific bias term $\beta_w^{(\text{nano})}(h^{-1})_r$. Unlike the complex oscillatory profile of the disjoining pressure, this term exhibits a simple, prominent positive ridge at the connection region. Crucially, its magnitude reaches $\mathcal{O}(10^{-7})$, exceeding the disjoining pressure contribution ($\mathcal{O}(10^{-9})$) by two orders of magnitude, which identifies this term as the dominant driver of the superspreading. Furthermore, the peak intensity of this bias flux decays over time, consistent with the experimental observation that the superspreading velocity gradually attenuates towards the later stages. This indicates that the nanoparticle-induced transport effectively overrides the classical lubrication dynamics.

4 Concluding remarks

This study demonstrates the capability of data-driven sparse modeling to elucidate the hidden physics of wetting dynamics from experimental data. To the best of our knowledge, this is the first application of such sparse identification techniques to experimental liquid-film profiles, specifically resolving the nanometer-thick precursor film—a regime where spatiotemporal measurements remain scarce. The identified partial differential equations successfully captured the distinct dynamics of pure and nanofluid spreading. Crucially, the discovery of a nanofluid-specific term provides a mathematical signature for the superspreading behavior. While the definitive physical mechanism behind nanofluid superspreading is yet to be fully resolved, the current data-driven technique may open new avenues for mechanistic investigation and the potential control of complex wetting dynamics.

Acknowledgements

K.F. acknowledges support from the JSPS KAKENHI Grant No. JP25K23418, the JST PRESTO Grant No. JP-MJPR25KA, and the MEXT Coordination Funds for Promoting Aerospace Utilization Grant No. JPJ000959. E.S. acknowledges support from the JSPS KAKENHI Grant No. JP24K01230. E.S. also acknowledges the Materials Processing Science Project (“Materealize”) of MEXT (Project No. JPMXP0219192801) for providing the nanoparticles used in our previous experiments.

Declaration of interests

The authors report no conflict of interest.

References

- [1] E. G. Schwarz and W. G. Reid. Surface-active agents — Their behavior and industrial use. *Ind. Eng. Chem.*, 56(9):26–31, 1964.
- [2] L. H. Tanner. The spreading of silicone oil drops on horizontal surfaces. *J. Phys. D Appl. Phys.*, 12(9):1473, 1979.
- [3] J. Venzmer. Superspreading – Has the mystery been unraveled? *Adv. Colloid Interface Sci.*, 288:102343–102343, 2021.
- [4] E. Shoji, A. Hoshino, T. Biwa, M. Kubo, T. Tsukada, T. Tomai, and T. Adschari. Superspreading wetting of nanofluid droplet laden with highly dispersed nanoparticles. *Langmuir*, 40(50):26509–26516, 2024.
- [5] A. D. Nikolov, D. T. Wasan, A. Chengara, K. Koczo, G. A. Policello, and I. Kolossvary. Superspreading driven by Marangoni flow. *Adv. Colloid Interface Sci.*, 96(1–3):325–338, 2002.
- [6] P. E. Theodorakis, E. A. Müller, R. V. Craster, and O. K. Matar. Superspreading: Mechanisms and molecular design. *Langmuir*, 31(8):2304–2309, 2015.
- [7] D. T. Wasan and A. D. Nikolov. Spreading of nanofluids on solids. *Nature*, 423(6936):156–159, 2003.
- [8] M. Z. Hossain, D. Hojo, A. Yoko, G. Seong, N. Aoki, T. Tomai, S. Takami, and T. Adschari. Dispersion and rheology of nanofluids with various concentrations of organic modified nanoparticles: Modifier and solvent effects. *Colloids Surf. A Physicochem. Eng. Asp., Coll. Surf. A*, 583:123876, 2019.
- [9] P. G. de Gennes. Wetting: statics and dynamics. *Rev. Mod. Phys.*, 57(3):827–863, 1985.
- [10] J. F Joanny and P. G. de Gennes. Upward creep of a wetting fluid: a scaling analysis. *Journal de Physique*, 47(1):121–127, 1986.
- [11] E. Shoji, A. Komiya, J. Okajima, M. Kubo, and T. Tsukada. Three-step phase-shifting imaging ellipsometry to measure nanofilm thickness profiles. *Opt. Laser Eng.*, 112:145–150, 2019.
- [12] S. H. Rudy, S. L. Brunton, J. L. Proctor, and J. N. Kutz. Data-driven discovery of partial differential equations. *Sci. Adv.*, 3(4):e1602614, 2017.
- [13] S. L. Brunton, J. L. Proctor, and J. N. Kutz. Discovering governing equations from data by sparse identification of nonlinear dynamical systems. *Proc. Natl. Acad. Sci. U.S.A.*, 113(15):3932–3937, 2016.
- [14] K. Champion, B. Lusch, J. N. Kutz, and S. L. Brunton. Data-driven discovery of coordinates and governing equations. *Proc. Natl. Acad. Sci. U.S.A.*, 116(45):22445–22451, 2019.

- [15] K. Fukami, T. Murata, K. Zhang, and K. Fukagata. Sparse identification of nonlinear dynamics with low-dimensionalized flow representations. *J. Fluid Mech.*, 926:A10, 2021.
- [16] H. K. Chu and M. Hayashibe. Discovering interpretable dynamics by sparsity promotion on energy and the Lagrangian. *IEEE Robot. Autom. Lett.*, 5(2):2154–2160, 2020.
- [17] N. M. Mangan, S. L. Brunton, J. L. Proctor, and J. N. Kutz. Inferring biological networks by sparse identification of nonlinear dynamics. *IEEE Trans. Mol. Biol. Multiscale Commun.*, 2(1):52–63, 2017.
- [18] A. A. Klishin, J. Bakarji, J. N. Kutz, and K. Manohar. Statistical mechanics of dynamical system identification. *Phys. Rev. Res.*, 7(3):033181, 2025.
- [19] I. Scherl, B. Strom, J. K. Shang, O. Williams, B. L. Polagye, and S. L. Brunton. Robust principal component analysis for modal decomposition of corrupt fluid flows. *Phys. Rev. Fluids*, 5(5):054401, 2020.
- [20] M. K. Hickner, U. Fasel, A. G. Nair, B. W. Brunton, and S. L. Brunton. Data-driven unsteady aeroelastic modeling for control. *AIAA J.*, 61(2):780–792, 2023.
- [21] E. Shoji, T. Kaneko, T. Yonemura, M. Kubo, T. Tsukada, and A. Komiya. Measurement of dynamic wetting using phase-shifting imaging ellipsometer: comparison of pure solvent and nanoparticle suspension on film thickness profile, apparent contact angle, and precursor film length. *Exp. Fluids*, 62(10):1–13, 2021.
- [22] E. Shoji, T. Saito, T. Biwa, M. Kubo, T. Tsukada, T. Tomai, and T. Adschariri. Transitions in intra-droplet flow and wetting governing nanoparticle deposition patterns in inkjet-printed nanofluids. *J. Colloid Interface Sci.*, 699:138246, 2025.
- [23] A. Oron, S. H. Davis, and S. G. Bankoff. Long-scale evolution of thin liquid films. *Rev. Mod. Phys.*, 69(3):931–980, 1997.
- [24] J. N. Israelachvili. *Intermolecular and surface forces*. Academic press, 2011.